Journal of Zhejiang University-SCIENCE C (Computers & Electronics)
ISSN 1869-1951 (Print); ISSN 1869-196X (Online)
www.zju.edu.cn/jzus; www.springerlink.com
E-mail: jzus@zju.edu.cn

A new maximum-likelihood phase estimation method for X-ray pulsar signals*

Hua ZHANG, Lu-ping XU, Yang-he SHEN, Rong JIAO, Jing-rong SUN

(*School of Aerospace Science and Technology, Xidian University, Xi'an 710126, China*)

E-mail: {zhanghua, lpxu}@mail.xidian.edu.cn; {yanghe_shen, jrong_06}@163.com; jrsun@xidian.edu.cn

Received Dec. 5, 2013; Revision accepted Apr. 22, 2014; Crosschecked May 4, 2014

Abstract: X-ray pulsar navigation (XPNAV) is an attractive method for autonomous navigation of deep space in the future. Currently, techniques for estimating the phase of X-ray pulsar radiation involve the maximization of the general non-convex object functions based on the average profile from the epoch folding method. This results in the suppression of useful information and highly complex computation. In this paper, a new maximum likelihood (ML) phase estimation method that directly utilizes the measured time of arrivals (TOAs) is presented. The X-ray pulsar radiation will be treated as a cyclo-stationary process and the TOAs of the photons in a period will be redefined as a new process, whose probability distribution function is the normalized standard profile of the pulsar. We demonstrate that the new process is equivalent to the generally used Poisson model. Then, the phase estimation problem is recast as a cyclic shift parameter estimation under the ML estimation, and we also put forward a parallel ML estimation method to improve the ML solution. Numerical simulation results show that the estimator described here presents a higher precision and reduces the computational complexity compared with currently used estimators.

Key words: X-ray pulsar, Poisson model, Phase estimation, Maximum likelihood
doi:10.1631/jzus.C1300347 **Document code:** A **CLC number:** TP273; V11

1 Introduction

Pulsars, especially millisecond pulsars (period below 20 ms), show extreme frequency stability of their pulse signals and they were proposed for use for positioning purposes as early as 1974 (Downs, 1974). In recent years, several studies have demonstrated the feasibility for a spacecraft to perform self-positioning based on the time of arrival (TOA) of the pulse radiated by pulsars (Sheikh, 2005; Ray *et al.*, 2006; Zhang and Xu, 2011; Zhang *et al.*, 2011).

Compared with other celestial sources, the radio pulsar is much more convenient for navigational use, given the timing precision allowed by radio pulsar timing. However, the radio emission from pulsars represents only a negligible fraction of their energy budget, and an efficient radio telescope is too big to be mounted on a spacecraft. In comparison, X-ray pulsars are interesting candidates for use in both absolute and relative navigation systems. This is because the X-rays carry a large part of the energy budget of pulsars, so a small and light X-ray detector can be employed for X-ray detection. Thus, X-ray pulsar navigation (XPNAV) has great potential for autonomous navigation in the exploration of deep space.

Autonomous navigation means that orbit determination is implemented solely on board and is independent of observation of the ground system. Space vehicles operating on a close-to-Earth orbit can also obtain an autonomous navigation solution that employs the well-known global navigation satellite

* Project supported by the National Natural Science Foundation of China (No. 61172138), the Fundamental Research Funds for the Central Universities (Nos. K5051302015 and K5051302040), the Natural Science Basic Research Plan in Shaanxi Province of China (No. 2013JQ8040), and the Research Fund for the Doctoral Program of Higher Education of China (No. 20130203120004)

systems (GNSS), such as the Global Positioning System (GPS), Global Navigation Satellite System (GLONASS), GALILEO, and COMPASS. Besides, in deep space where the GPS signal is not available, the deep space network (DSN) can be used for deep space missions. However, in a sense, none of these methods can determine the orbit autonomously because such GNSS systems and DSN rely on observation of a ground-based system. To obtain complete solutions or augment current systems, some natural sources such as the magnetic field (Bar-Itzhack and Oshman, 1985), Sun (Psiaki, 2011), star (Ma, 2005; Chubei *et al.*, 2007), and ultraviolet (Billing-Ross *et al.*, 1992) are employed to obtain additional measurements. These natural sources cannot provide high precision and have application restrictions subject to their natural limitations on spatial and temporal observation. By comparison, except for the observability all over the solar system, X-ray pulsar based navigation (Sheikh *et al.*, 2007; Ashby and Golshan, 2008; Ray *et al.*, 2008; Emadzadeh and Speyer, 2011) can provide precise orbit determination through time or phase measurement, which is another kind of 'natural GPS' obtaining a fully autonomous solution.

Recently, several researchers have investigated different applications of XPNAV for both absolute navigation (Sala *et al.*, 2004; Sheikh *et al.*, 2007) and relative navigation (Emadzadeh and Speyer, 2011). It has been shown that one key issue of XPANV is how to precisely measure the TOA of the X-ray pulses. Hanson *et al.* (2008) proposed an epoch folding method for phase estimation, based on the assumption that the underlying signals are Gaussian. Emadzadeh and Speyer (2010) improved those results, and formulated the epoch folding procedure mathematically. Also, Emadzadeh and Speyer (2010) designed a nonlinear least-squares (NLS) estimator for the pulse phase and a maximum likelihood pulsar phase estimator based on a statistical model of the TOAs of photons. They also studied its performance against the Crámer-Rao lower bound. Both estimators employ the grid discretization searching method in the direct search maximization procedure, which achieves a tradeoff between computation complexity and estimation accuracy. Some researchers improved this method and proposed a fast near-maximum likelihood method based on the generalized method of moments (GMM) approach (Colonnese *et al.*, 2010; Rinauro *et al.*, 2013). Li and Ke (2011) described a low signal-to-noise ratio (SNR) pulsar phase estimator. The low SNR approximation allows us to reduce computation complexity, but causes estimator performance to degrade with increased SNR values. Ray *et al.* (2011) presented three methods of Gaussian kernel density estimation (KDE), i.e., the empirical Fourier (EF), the sum of the Gaussian peaks to describe the pulsar profile template, and a maximum likelihood TOA determination method for gamma-ray pulsar timing. This method estimates the TOA from a set of phases obtained by folding the photon arrival times, and it can also be used in the TOA measurement of the X-ray pulsar (Ray *et al.*, 2011).

In this paper, we treat the phase estimation of the pulsar signal as a general cyclic shift parameter estimation problem under multinomial distributed observations. In our previous work, the multi-component Gaussian fitting method was used to unambiguously and uniquely determine profile characteristics such as the width of the profile and the numbers and positions of components (Zhang and Xu, 2011; Zhang *et al.*, 2011). In the following sections, after introducing the basic signal model of the X-ray pulsar, we will show that the commonly used Poisson model can be approximated by a multi-component Gaussian distribution. Then we illustrate how to form an approximate, computationally efficient, maximum likelihood (ML) pulsar signal phase estimator. In addition, the Crámer-Rao lower bound is presented to evaluate the performance of the X-ray pulsars in phase and velocity estimation.

2 Poisson model of X-ray pulsar signals

The original measurement of the X-ray pulsar is the high energy photon rate emitted by the source. This rate can be measured in terms of the flux of radiation, or the number of photons per unit area per unit time. Given the energy range of photons being observed, the total number of photons can be converted to energy. Comparatively, since the photons arrive at the detector one by one, the TOA can precisely define the photon. Thus, in this study, the photon TOAs are used to form an analytical model of the X-ray pulsar signals. Since the actual X-ray

detector measures the TOAs of photons when they hit the detecting material, we construct a time sequence model based on Poisson distribution.

2.1 Time sequence model of X-ray pulsar signals

Due to its high cyclic stability, X-ray pulsar radiation can be characterized by a cyclo-stationary process. As above indicated, the nature of the received photons can be expressed in terms of a Poisson point process.

Let t_0 be the reference time and t_E the end time of one observation. We use $\{T_i\}_{i=1}^{E}$ to denote the ith sampling interval, where $T_i=t_i-t_{i-1}$. The number of photons of X-ray pulsar radiation falling into T_i is a random variable obeying a Poisson distribution. The probability that k Poisson points fall into the interval of time T_i is provided by the following relationship (Sala *et al.*, 2004; Emadzadeh and Speyer, 2010):

$$p(k=k_n)=\frac{1}{k_n!}\left(\int_{T_i}\lambda(t)\mathrm{d}t\right)^{k_n}\exp\left(\int_{T_i}-\lambda(t)\mathrm{d}t\right), \quad (1)$$

where $\lambda(t)$ represents the nonuniform density of X-ray pulsar radiation and we have $\int_{T_i}\lambda(t)\mathrm{d}t \underset{T_i\to 0}{\approx} \lambda(t)T_i$. $\lambda(t)T_i$ closely relates to pulse phase evolution and the pulse profile, which will be discussed in the following sections. Using the determined pulse frequency f and its derivatives, the total phase can be specified at a specific location using a pulsar phase model. Even though some normal pulsars are sometimes subjected to 'timing noise' and 'glitches' (Hobbs *et al.*, 2006), the stability of rotation for carefully selected pulsars for navigation is remarkable, especially for the milli-second pulsars. At the reference frame of the solar system barycenter (SSB), the phase evolution of the pulsar signal is expressed as follows (Manchester and Taylor, 1977; Lyne and Smith, 1998; Sala *et al.*, 2004):

$$\Phi_n^{\mathrm{SSB}}(t)=\Phi_n^{\mathrm{SSB}}(t_0)+f_n\cdot(t-t_0)+O(m), \quad (2)$$

where $\Phi_n^{\mathrm{SSB}}(t)$ is the phase evolution of the nth pulsar at a generic time t, f_n is the pulse frequency of the nth pulsar, and $O(m)$ is the high-order item of $\Phi_n^{\mathrm{SSB}}(t)$. $O(m)$ can be expressed by

$$O(m)=\sum_{m=2}^{M}\frac{f_n^{(m)}\cdot(t-t_0)^m}{m!}, \quad (3)$$

where $f_n^{(m)}$ is the mth order derivative of the frequency and is derived by observing the nth pulsar for a long time. Since the high order terms barely have effects on the phase in a short time, we can consider $O(m)$ an insignificant variable and thus its effect on phase evolution is negligible. In order to further simplify the expression, φ is used to substitute for $\Phi_n^{\mathrm{SSB}}(t)$.

The velocity of the detector results in a Doppler frequency f_d, which can be decomposed into two different components: X-ray source frequency f_0 and Doppler frequency shift $f_0\cdot v/c$. In other words,

$$f_v=f_0\cdot(1+v/c), \quad (4)$$

where v is the velocity of the detector, c is the velocity of light. Consequently, assuming $\varphi_v(t)$ is the observed phase and the velocity of the detector is a constant, the detected phase is

$$\varphi_v=\varphi_{x_0}+f_v\cdot(t-t_0), \quad (5)$$

where x_0 is the original position of the detector, and φ_{x_0} is the initial phase.

During the navigation process, an X-ray pulsar has a unique and stable integrated pulse profile associated with the pulse phase. We use $h(\varphi)$ to represent the normalized pulse profile, and λ_b and λ_s to denote the effective background and the source count rate, respectively. In addition, the effective area of the detector (A), the number of waveforms folded (K), and the detector efficiency (η) are associated with the model (Hanson *et al.*, 2008). Based on Eq. (5), the model of the arrival rates of X-ray pulsars can be expressed as the function of the profile:

$$\begin{aligned}\lambda(T_i;\varphi_v,v)&=\int_{T_i}AK\eta(1+v/c)(\lambda_\mathrm{b}+\lambda_\mathrm{s}h(\varphi_v))\mathrm{d}t\\&\approx AK\eta(\lambda_\mathrm{b}+s\cdot h(\varphi_v))T_i,\end{aligned} \quad (6)$$

where T_i is the ith sampling interval, x is the reference point, v is the velocity of the detector, λ_s is the scale factor corresponding to the X-ray pulsar signal

radiation intensity, and $h(\varphi_v)$ is the dc-removed normalized profile of the pulsar due to the motion of the detector toward the source. More details of the influence of the velocity can be found in Emadzadeh and Speyer (2010) and Zhang *et al.* (2011).

Since T_i is a non-overlapping time interval, k_n, i.e., a photon falling into T_i, obeys an independent Poisson distribution, which can be represented as follows:

$$p_i(k_n;\varphi_v,v)=\frac{\lambda(T_i;\varphi_v,v)^{k_n}}{k_n!}\exp(-\lambda(T_i;\varphi_v,v)), \quad (7)$$

where k_n=1, 2, …. For the Poisson distribution shown in Eq. (7), its mean and variance are

$$E(k_n)=\mathrm{var}(k_n)=\lambda(T_i;\varphi_v,v). \quad (8)$$

For time sequence $\{T_i\}_{i=1}^{E}$, the joint probability mass function of the sequence can be expressed as

$$p(k_n/\varphi_v,v)=\prod_{n=1}^{N}\frac{\lambda(T_i;\varphi_v,v)^{k_n}}{k_n!}\exp(-\lambda(T_i;\varphi_v,v)). \quad (9)$$

3 New model of pulsar digital signals

Several papers have discussed the TOA estimation of the X-ray pulsar signals through the average profile using the epoch folding method (Emadzadeh and Speyer, 2010; Zhang and Xu, 2011; Zhang *et al.*, 2011). However, the average profile suppresses some useful information about the parameters that may be contained in the photon TOAs. To directly utilize the measured TOAs, a new X-ray pulsar signal model and an ML estimator are presented and formulated. We also prove that the new model is equivalent to the aforementioned Poisson model.

3.1 New model of the photon sequence

Assume that the recorded data starts at t_0, and let t_{end} denote the end time. Then, the observation interval is $t_{\mathrm{obs}}=t_{\mathrm{end}}-t_0$. Furthermore, let t_i denote the TOA of the ith photon and the photon sequence can be expressed as $\{t_i\}_{i=1}^{m}=\{t_1,t_2,...,t_m\}$. The definition of the model mentioned in Section 2.1 indicates that the recorded sequence arrives in ascending order (Emadzadeh and Speyer, 2010). That is,

$$t_0\le t_1<t_2<t_3<\cdots<t_m\le t_{\mathrm{end}}. \quad (10)$$

From recent literature (Emadzadeh and Speyer, 2010; Zhang *et al.*, 2011), we note that due to the weaknesses of pulsar signals, XPNAV must use the statistical arrival time of all observed photons to determine the position of the spacecraft. From this point of view, some average methods such as the epoch folding method have been proposed (Hanson *et al.*, 2008; Emadzadeh and Speyer, 2010). The epoch folding method folds all the time tags during the observation time back into a single time interval equal to one pulse period. By this we can assume that, for the pulsar photon sequence, n photons being captured in one period can be considered the independent event of one photon, whose probability distribution function is the normalized pulsar profile, theoretically occurring n times in the period. This hypothesis is supported by the theorem given as follows:

Theorem 1 Let $h(\varphi)$ denote the normalized pulsar profile, that is, $\int_0^1 h(\varphi)d\varphi=1$. Suppose there is only one photon in one pulsar period. Its arrival time follows the distribution with a probability distribution function $h(\varphi)$.

Proof Without loss of generality, we assume λ_b=0. Then, according to Eq. (6), the pulsar signal density can be rewritten as $\lambda_{\mathrm{s},\Delta}=\int_{\Delta}AK\eta\lambda_{\mathrm{s}}h(\varphi)\mathrm{d}\varphi$, where Δ is the time interval between the start time of the period and the TOA of the photon. Let P be the period of the pulsar. If there is one photon arriving in P, the probability of this event in interval Δ can be given by

$$\begin{aligned}p(x(\Delta)=1\,|\,x(P)=1)&=\frac{p(x(\Delta)=1,x(P)=1)}{p(x(P)=1)}\\&=\frac{p(x(\Delta)=1,x(P-\Delta)=0)}{p(x(P)=1)}\\&=\frac{\lambda_{\mathrm{s},\Delta}\mathrm{e}^{-\lambda_{\mathrm{s},\Delta}}}{\lambda_{\mathrm{s},P}\mathrm{e}^{-\lambda_{\mathrm{s},P}}}\mathrm{e}^{-\lambda_{\mathrm{s},(P-\Delta)}}=\frac{\int_{\Delta}h(\varphi)\mathrm{d}\varphi}{\int_{P}h(\varphi)\mathrm{d}\varphi}.\end{aligned} \quad (11)$$

Furthermore, because $\int_P h(\varphi)\mathrm{d}\varphi=1$, we have $p(x(\Delta)=1\,|\,x(P)=1)=\int_{\Delta}h(\varphi)\mathrm{d}\varphi$. It is easy to find

that the probability density of the instant time τ of the event in a period is

$$p(\tau) = h(\tau). \tag{12}$$

Therefore, Theorem 1 is proved.

Based on Theorem 1 and Eq. (12), a new generation method is proposed to detect the pulsar signal. Let τ_n denote the fractional part of the nth photon time, and N the cycle count. We have

$$\tau_n = (t_i - NP) / P. \tag{13}$$

If the pulsar frequency is an unknown quantity due to the velocity of the spacecraft, the period should be amended as

$$\tau_n = (t_i - NP_v) / P_v, \tag{14}$$

where P_v=Pc/(c+v) according to Eq. (4), and v is the velocity of the spacecraft. Thus, according to Theorem 1, the probability of the TOAs of the photons in one period can be restated as

$$p(\tau_n) = h_g(\tau_n), \quad \tau_n \in [0,1). \tag{15}$$

Eq. (15) indicates that the distribution of the photon TOAs in the Nth cycle can be approximated using the normalized standard profile as the distribution function.

In comparison with the Poisson model given in Section 2.1 (Emadzadeh and Speyer, 2010; Ray *et al.*, 2011; Rinauro *et al.*, 2013), the model here has three distinct characteristics: (1) The new model describes the photons using their TOAs along the time axis instead of the intensity in the Poisson model; (2) The new model does not need to divide the photon sequence into bins of the same length; (3) The probability function of the new model is the normalized profile of the pulsar, so different pulsars have different probability functions.

3.2 Multi-Gaussian fitting of X-ray pulsar profiles

The shapes of the averaged pulsar profiles are very stable, providing valuable information about the physical process of radio emission from pulsars (Xu and Wu, 2003). Rankin *et al*. (1990) found that there is a central component in the emission beam and classified the mean pulse profiles into different categories, i.e., single-, double-, triple-, quadruple-, and five-component, after analyzing various profiles and their polarization properties. Consequently, Rankin *et al*. (1990) proposed that the emission beam is composed of a central core component and two peripherally homocentric hollow cones, based on which the author proposed the core-double-cone model. Based on this model, Xu and Wu (2003) fitted the integral profile using multi-Gaussian functions and advanced the Gaussian fit separation of the average profile (GFSAP) method to express the pulsar profile. Through investigating 200 profiles of 18 pulsars obtained from a 100-m radio telescope of the MPifR in Effelsberg, Kramer (1994) found that GFSAP fits the individual components well.

Ray *et al.* (2011) presented three methods, i.e., Gaussian kernel density estimation (KDE), empirical Fourier (EF), and the sum of Gaussian peaks, to describe the γ pulsar profile template. The fitting method in KDE is similar to that in GFSAP.

Except for its physical significance, GFSAP is good at representing the pulsar profiles' structure and minutiae. Thus, we describe this method by fitting the sum of Gaussian functions

$$h_g(\varphi_v) = \sum_{i=1}^{M} f_i(\varphi_v) \tag{16}$$

to the normalized average pulsar profile. In Eq. (16),

$$f_i(\varphi_v) = a_i \frac{1}{\sqrt{2\pi\delta_i^2}} \exp\left[-\frac{(\varphi_v - \mu_i)^2}{\delta_i^2} \right], \tag{17}$$

where a_i, μ_i, and δ_i are the scale factor, mean, and variance of the ith Gaussian component, respectively.

To define the initial phase φ_0, we can rewrite Eq. (17) as

$$f_i(\tau_n) = a_i \frac{1}{\sqrt{2\pi\delta_i^2}} \exp\left\{ -\frac{[\tau_n - (\varphi_0 + \delta\mu_i)]^2}{\delta_i^2} \right\}, \quad i = 1, 2, \cdots, M, \tag{18}$$

where μ_i=φ_0+$\delta\mu_i$, and $\delta\mu_i$ is the offset between the initial phase and the ith part of the pulsar profile. In general, φ_0 can be set to an arbitrary value in [0, 1). In the following, we set φ_0=μ_0, which means $\delta\mu_0$=0.

4 Phase estimator using the GFSAP model

4.1 ML estimator of the initial phase

Employing the new probability model from Section 3.1, an ML estimation problem can be formulated to estimate φ_0. According to Eqs. (15) and (18), the pdf of the sequence is given by

$$p(\{t_i\}_{i=1}^m;\varphi_0)=\prod_{i=1}^m h_{\mathrm{g}}(\tau_i;\varphi_0). \tag{19}$$

Taking the pdf given in Eq. (19) as the likelihood function, the ML estimator is provided by maximizing Eq. (19) with respect to the unknown parameter φ_0. Equivalently, the natural logarithm of the likelihood function can be maximized:

$$\mathrm{LLF}(\varphi_0)=\sum_{i=1}^m \ln h_{\mathrm{g}}(\tau_i;\varphi_0), \tag{20}$$

where LLF means the log-likelihood function. Then, the initial phase can be estimated by solving the following optimization problem:

$$\hat{\varphi}_0=\underset{\varphi_0\in[0,1)}{\operatorname{argmax}}\,\mathrm{LLF}(\varphi_0). \tag{21}$$

4.2 Estimation of the period

If the period P is an unknown quantity, it can also be estimated using the proposed ML estimator. In this case, P and the initial phase φ_0 are the variables of the cost function:

$$\mathrm{LLF}(\varphi_0,P_v)=\ln h_{\mathrm{g}}(\tau_n;\varphi_0,P_v), \tag{22}$$

and the unknowns can be found by solving

$$(\hat{\varphi}_0,\hat{P}_v)=\underset{\varphi_0\in[0,1),P_v\in\Gamma}{\operatorname{argmax}}\,\mathrm{LLF}(\varphi_0,P_v), \tag{23}$$

where Γ is the searching space of P_v.

4.3 Performance of the ML estimator

Based on the time sequence model of the X-ray pulsar and the multi-Gaussian fitting of the profile, the Cramer-Rao lower bound (CRLB) of the initial phase, the period estimation, and the pulsar quality factor are all presented in this section. The CRLB is a lower bound on the variance of any unbiased estimator of unknown parameters. It is a valid, tight, and lower bound to the performance of the estimation algorithms (such as ML) in a small error region. Let $p(\boldsymbol{\tau}_n;\boldsymbol{\theta})$ be the pdf of the observed random vector $\boldsymbol{\tau}_n$, which is parameterized by the unknown parameter $\boldsymbol{\theta}=[\varphi_0, P_v]^{\mathrm{T}}$. Then the Fisher information of $\boldsymbol{\theta}$, $J(\boldsymbol{\theta})$, can be expressed as

$$J(\boldsymbol{\theta})=-E\left(\frac{\partial^2 \log_2 p(\boldsymbol{x};\boldsymbol{\theta})}{\partial\boldsymbol{\theta}^2}\right), \tag{24}$$

which assumes that $p(\boldsymbol{x};\boldsymbol{\theta})$ satisfies the 'regularity' condition, i.e.,

$$\int\frac{\partial p(\boldsymbol{x};\boldsymbol{\theta})}{\partial\boldsymbol{\theta}}\mathrm{d}x=0. \tag{25}$$

The CRLB of the unbiased vector estimation of $\boldsymbol{\theta}$ is given by

$$\mathrm{cov}(\hat{\boldsymbol{\theta}})\geq J^{-1}(\boldsymbol{\theta}). \tag{26}$$

For phase φ_v, the Fisher information is given by

$$J(\varphi_v)=-\sum_{i=1}^N\frac{1}{\lambda(T_i;\boldsymbol{\theta})}\left(\frac{\partial\lambda(T_i;\boldsymbol{\theta})}{\partial\varphi_v}\right)^2. \tag{27}$$

In a similar manner, the Fisher information of velocity v is given by

$$J(v)=-\sum_{i=1}^N\frac{1}{\lambda(T_i;\boldsymbol{\theta})}\left(\frac{\partial\lambda(T_i;\boldsymbol{\theta})}{\partial v}\right)^2. \tag{28}$$

Since $\lambda(\cdot)$ is a periodic function, after some derivation (for details, see the Appendix), the CRLB for phase and velocity can be expressed as

$$\mathrm{CRLB}(\varphi_0)=\left(\frac{AK\eta\lambda_{\mathrm{s}}^2 f_0^2}{Pc}t_{\mathrm{obs}}T_i\Omega\right)^{-1}, \tag{29}$$

$$\mathrm{CRLB}(v)=\left(\frac{AK\eta\lambda_{\mathrm{s}}^2 f_0^2}{3Pc^2}T_{\mathrm{obs}}^3T_i\Omega\right)^{-1}, \tag{30}$$

where t_{obs} is the observation time, P is the period of the pulsar, c is the speed of light, and

$$\Omega=\sum_{k=1}^{M}\sum_{j=1}^{M}\frac{C_M^k}{\delta_k^2\delta_j^2}\int_0^P\frac{\varphi_v^2 f_k(\varphi_v)f_j(\varphi_v)}{\lambda_b+\lambda_s\cdot h_g(\varphi_v)}\mathrm{d}\varphi_v, \quad (31)$$

where $C_M^K=\dfrac{M!}{K!(M-K)!}$. Eq. (29) shows that CRLB(φ_0) is proportional to the pulse period and inversely proportional to effective area A, detector efficiency η, quadratic flux λ_s^2, observation time T_{obs}, sampling time interval T_i, quadratic pulse frequency f_0^2, and the factor of profile Ω. Compared with Eq. (29), most parameters of CRLB(v) shown in Eq. (30) are the same, except that CRLB(v) is inversely proportional to $T_{obs}^3/3$. As shown by Eq. (31), based on the multi-Gaussian fitting method, the contribution of the pulse profile to CRLB is related to the variance multiplication, i.e., $\delta_k\delta_j$, and $f_k(\cdot)f_j(\cdot)$ is the correlation of every component. It is shown that, to obtain higher navigation performance or a lower CRLB, the pulsar profile that has less $\delta_k\delta_j$ or greater $f_k(\cdot)f_j(\cdot)$ should be employed, and the pulsar profiles with more components are more likely to perform better in estimations.

The derivation of Eqs. (29) and (30), provided in the Appendix, refers to our previous work (Zhang and Xu, 2011).

4.4 Numerical searching method

In general, the GFSAP model must use multiple Gaussian components to fit a pulsar profile which has multiple peaks. Therefore, the cost function is not generally convex; instead, it usually has multiple minima. To avoid getting trapped in local extremes, the grid discretization searching method can be employed in the direct search maximization procedure. This method arises from a tradeoff between computational complexity and accuracy of estimation. Considering the phase estimation generally used in the iterative position determination procedure, the priori phase information can be acquired easily from the previously determined position. Therefore, the Newton-Raphson iteration searching method can be used, whose iteration factor is given by

$$\boldsymbol{\theta}_{k+1}=\boldsymbol{\theta}_k+[J(\boldsymbol{\theta})]^{-1}\mathrm{pLLF}(\boldsymbol{\theta})\big|_{\boldsymbol{\theta}=\boldsymbol{\theta}_k}, \quad (32)$$

where k=0, 1, 2, …, $\mathrm{pLLF}(\boldsymbol{\theta})=\dfrac{\partial\ln p(\{t_i\}_{i=1}^m;\boldsymbol{\theta})}{\partial\boldsymbol{\theta}}$. The iteration process terminates when $\|\boldsymbol{\theta}_{k+1}-\boldsymbol{\theta}_k\|<\xi$, where ξ is the convergence threshold. For details of the Newton-Raphson iteration, refer to Kay (1998). However, for a long observation time, pLLF($\boldsymbol{\theta}$) in Eq. (32) uses significant computational resources. This is because, for every photon TOA, a nonlinear Gaussian sum function must be calculated. The next subsection presents two methods for improving computational efficiency.

4.5 Improving the searching performance

Two methods can be employed to reduce complexity. The first is linear interpolation of pLLF($\boldsymbol{\theta}$). In this method, the definition domain of the partial derivative is subdivided into several equi-spaced bins; when the photon TOA falls into the corresponding bin, the interpolation function is used as a substitute for the partial derivative.

The second method is parallel computation of pLLF($\boldsymbol{\theta}$). Since the proposed model in Section 3 assumes that the X-ray pulsar signals are cyclo-stationary processes, all the photon TOAs have the same probability distribution function. Thus, pLLF($\boldsymbol{\theta}$) can be recast as

$$\mathrm{pLLF}(\boldsymbol{\theta})=\sum_{l=1}^{L}\sum_{i=la+1}^{la+a}\frac{\partial\ln h_g(\tau_n;\boldsymbol{\theta})}{\partial\boldsymbol{\theta}}. \quad (33)$$

Eq. (33) means that the calculation process can be divided into L independent subprocesses and each subprocess has a photons. According to Eq. (33), pLLF($\boldsymbol{\theta}$) can be calculated using the following three steps (Fig. 1):

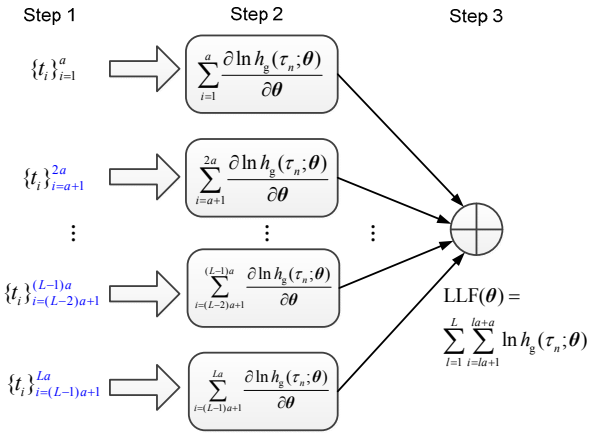

Fig. 1 Schematic of the parallel strategy

1. Subdivide the photon sequence into L parts. Every part contains $[m/L]$ photons, where $[\cdot]$ represents the rounding operation.

2. For every part in step 1, calculate the pLLF function.

3. Add all the results obtained in step 2.

5 Numerical simulation

Three pulsars, B0531+21, B1937+21, and B0329+54, whose parameters are as given in Table 1, are used to test the three proposed methods (Sheikh, 2005). The profile of the three pulsars can be fitted by a multi-Gaussian method. As an example, the multi-Gaussian fitting of pulsar B0531+21 is presented in Table 2 and plotted in Fig. 2. The standard profle in Fig. 2 is generated by FTOOLS (Blackburn *et al*., 1993) using data from the RXTE X-ray telescope.

The simulations are performed using a Monte Carlo technique with over 100 independent realizations of TOAs for each observation time. Referring to Sheikh (2005) and Sheikh and Pines (2006), we assume that the detector area A is 1 m^2 and the background photon rate is λ_b=0.05 ph/(s·cm^2). The photon arrival flux λ_s is shown in Table 1, and the photons are measured within the energy range 2–10 keV. The initial phase is chosen to be $\varphi_0=160\pi\rho$, where ρ is the length of the equal-length bin of the profile samples.

The procedure for ML estimation simulation is as follows. First, based on the assumed parameters, namely detector area A, background photon rate λ_b, and source arrival rate λ_s, the amount and TOA of the detected photon rates are generated. Second, substituting the TOAs into the cost function presented in Eq. (20), the initial phase $\hat{\varphi}_0$ can be estimated by solving Eq. (21). Then, using the Monte Carlo technique, we can obtain 100 estimated initial phases $\hat{\varphi}_0$ for each observation time. The mean square error (MSE) is defined as follows:

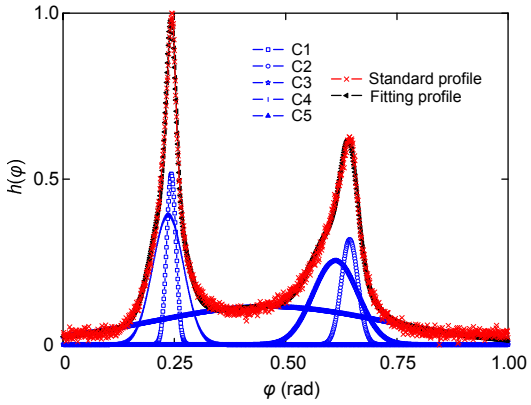

Fig. 2 Multi-Gaussian fitting of pulsar B0531+21

$$\mathrm{MSE}(\hat{\varphi}_0)=E[(\hat{\varphi}_0-\varphi_0)^2]. \tag{34}$$

The MSE of the 100 estimated initial phases can be easily derived. Finally, as the observation time changes from 1 to 500 s, the root mean square (RMS) of the ML estimation error can be obtained.

The parallel ML estimator simulation is generally similar to the current ML estimation, except for the construction of the cost function pLLF($\boldsymbol{\theta}$) described in Section 4.5. The parallel computation of

Table 1 Parameter of the three pulsars employed

Pulsar	Period (s)	Sampling interval (s)	Flux* (ph/(s·cm^2))	Qualification factor
B0531+21	0.0335	5.3e-4	1.54e+0	1.1601e+10
B1937+21	0.0016	1.5e-6	4.99e-5	4.7026e+5
B0329+54	0.7145	1.5e-3	5.15e-3	2.1275e+2

* The photons are measured within the energy range 2–10 keV

Table 2 Parameter of multi-Gaussian fitting of pulsar B0531+21

Gaussian component	Mean	Variance	Scale	Gaussian component	Mean	Variance	Scale
C1	3.584e-1	1.708e-2	4.298e-3	C4	3.322e-1	3.801e-3	7.340e-4
C2	3.765e-1	3.581e-3	8.660e-4	C5	3.500e-1	4.533e-3	1.603e-3
C3	3.572e-1	3.971e-3	8.826e-3				

pLLF($\boldsymbol{\theta}$) in the parallel ML estimator reduces the computational complexity. In this simulation, to show the superiority of the parallel ML estimator, we use independent parallel sub-processes with the same amount of arrival time to estimate the phase.

The NLS estimator simulation is illustrated in comparison with the ML estimator and the improved ML estimator. First, the generation of TOA is the same as that of the ML estimator. Second, knowing the TOA of the detected photon, the average profile is obtained using the epoch folding method. Then we can obtain the estimated initial phase $\hat{\varphi}_0$ by maximizing the correlation function of the average profile and the standard profile. Using the Monte Carlo technique, the MSE of 100 estimated initial phases $\hat{\varphi}_0$ is calculated for each observation time. Finally, changing the observation time from 1 to 500 s, the RMS of the NLS estimation error can be obtained.

In Fig. 3, the cost functions of the three pulsars are plotted. It can be seen that the three pulsars have different extremes. It is also known that pulsars B0531+21 and B1937+21 have multiple extremes. As a result, a numerical searching method is applied to avoid getting trapped in local extremes.

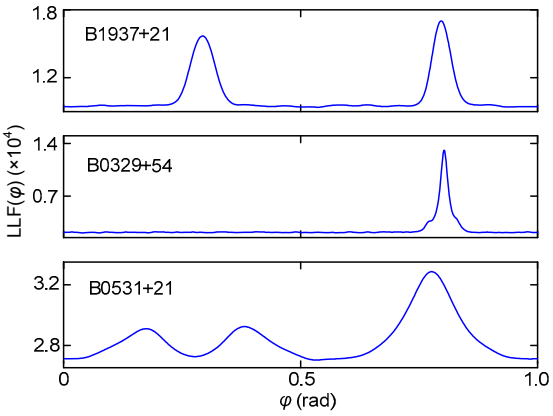

Fig. 3 Cost functions of three pulsars

Fig. 4 shows the RMS of the ML estimator, the RMS of the NLS estimator, and the square root of CRLB(φ_0) for each observation time. The ML estimator and the NLS estimator are both asymptotically unbiased, compared with the CRLB(φ_0) presented in Eq. (29), and the ML estimator is more asymptotically efficient than the NLS estimator. As observation time decreases, the RMS of both ML and NLS estimators deviates from CRLB(φ_0) below the threshold point; in contrast, they follow a more and more unbiased trend above the threshold point.

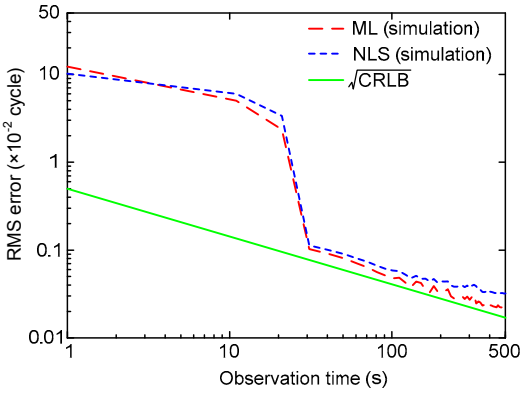

Fig. 4 RMS errors of different simulation methods

The ML proposed by Emadzadeh *et al.* (2011) using the direct searching procedure employs grid discretization. The overall computational complexity is approximately $N_{\text{obs}}[1+6/(f_0T_i)]$ MAC (multiplication-accumulation computation) (Benedetto *et al.*, 2013), where N_{obs} is the total number of photons. The computational cost is proportional to the number of received photons, and it can become significantly large for a long observation time. Furthermore, to achieve high precision, T_i should be small enough. Generally, T_i is close to 1 μs, which results in high computational complexity. Taking pulsar B0531+21 as an example, for a 500 s photon sequence there is about 2.5×10^{10} MAC. Our method uses the numerical searching method instead of the grid discretization method. Monte Carlo simulations show that generally fewer than 50 iterations are needed for the curves in Fig. 4 to converge. So, the computational complexity of our method is generally less than $51N_{\text{obs}}$. The computational complexity of the fast near-maximum likelihood method proposed by Benedetto *et al.* (2013) is $N_{\text{b}}(N_0+1)+N_{\text{b}}(2\log_2 N_{\text{b}}+1)$, where N_{b} is the number of sampling bins in one period and N_0 is the number of cycles. It is not difficult to find that if $N_{\text{obs}}>>N_{\text{b}}$, the fast near-maximum likelihood method is faster than the direct searching procedure and our method. However, our method can be easily applied in practice and implemented using the parallel method. It is very suitable for FPGA.

Although the current ML estimator is superior to the NLS estimator on the asymptotically unbiased side, the operation time taken by the estimator should

be considered. Fig. 5 shows the CPU time that Matlab R2011b takes for one Monte Carlo realization, as a function of the observation time. The processor used is a computer with an Intel 3.2 GHz quad-core and the Windows 7 operating system. The ML estimator takes more time than the NLS estimator, while the parallel ML estimator spends less time with the change of the parallel subprocess number L. In this simulation, L has three different values, namely 2, 10, 20. When L is set to 2, the CPU time decreases, but still larger than that of the NLS estimator. When L is set to 10, the parallel ML estimator takes almost the same time as the NLS estimator does. When L is set to 20, the time taken by the parallel estimator is less than that of the NLS estimator. As a result, the NLS estimator has significantly reduced the computational complexity compared with the current ML estimator.

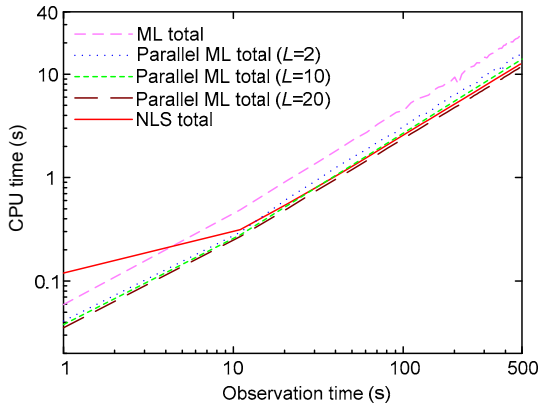

Fig. 5 CPU time of different simulation methods

6 Conclusions

X-ray pulsar signals were analyzed using a mathematical model and a new process of TOA was defined. We used the maximum likelihood method to estimate the signal phase. A parallel ML estimation method was developed and compared with the current ML estimator and the NLS estimator. It was shown that the current ML estimator and the parallel ML estimator were both more asymptotically efficient than the NLS estimator. However, the current ML estimator was computionally more expensive than the NLS estimator. Since the parallel ML estimator reduced computional complexity more than the current ML estimator did, it spent less time than the NLS estimator did when the photons were divided into specifically independent parallel subprocesses. As a result, the parallel estimator has advantages over the NLS estimator, not only in asymptotically unbiased estimation, but in computational complexity.

References

Ashby, N., Golshan, A.R., 2008. Minimum uncertainties in position and velocity determination using X-ray photons from millisecond pulsars. Proc. Institute of Navigation, National Technical Meeting, p.110-118.

Bar-Itzhack, I.Y., Oshman, Y., 1985. Attitude determination from vector observations: quaternion estimation. *IEEE Trans. Aerosp. Electron. Syst.*, **AES-21**(1):128-136. [doi:10.1109/TAES.1985.310546]

Benedetto, F., Giunta, G., Lohan, E.S., *et al.*, 2013. A fast unambiguous acquisition algorithm for BOC-modulated signals. *IEEE Trans. Veh. Technol.*, **62**(3):1350-1355. [doi:10.1109/TVT.2012.2228681]

Billing-Ross, J., Fritz, T., Pledger, D., 1992. Ultraviolet three axis attitude sensor. Annual AIAA/Utah State University Conf. on Small Satellites, p.1-5.

Blackburn, J.K., Greene, E.A., Pence, W., 1993. FTOOLS: a FITS data processing and analysis software package. *Bull. Am. Astron. Soc.*, **25**:816.

Chubei, M.S., Kovalchuk, L.V., Kholodova, S.I., *et al.*, 2007. Star sensor for independent navigation in deep space. *J. Opt. Technol.*, **74**(2):107-114. [doi:10.1364/JOT.74.000107]

Colonnese, S., Rinauro, S., Scarano, G., 2010. Generalized method of moments estimation of location parameters: application to blind phase acquisition. *IEEE Trans. Signal Process.*, **58**(9):4735-4749. [doi:10.1109/TSP.2010.2050316]

Downs, G.S., 1974. Interplanetary Navigation Using Pulsating Radio Sources. N/4-34150. NASA Technical Reports.

Emadzadeh, A.A., Speyer, J.L., 2010. On modeling and pulse phase estimation of X-ray pulsars. *IEEE Trans. Signal Process.*, **58**(9):4484-4495. [doi:10.1109/TSP.2010.2050479]

Emadzadeh, A.A., Speyer, J.L., 2011. Relative navigation between two spacecraft using X-ray pulsars. *IEEE Trans. Contr. Syst. Technol.*, **19**(5):1021-1035. [doi:10.1109/TCST.2010.2068049]

Hanson, J., Sheikh, S., Graven, P., *et al.*, 2008. Noise analysis for X-ray navigation systems. Position, Location and Navigation Symp., IEEE/ION, p.704-713. [doi:10.1109/PLANS.2008.4570028]

Hobbs, G., Lyne, A., Kramer, M., 2006. Pulsar timing noise. *Chin. J. Astron. Astrophys.*, **6**(S2):169-175. [doi:10.1088/1009-9271/6/S2/31]

Kay, S.M., 1998. Fundamentals of Statistical Signal Processing, Volume 1: Estimation Theory. Prentice Hall PTR.

Kramer, M., 1994. Geometrical analysis of average pulsar profiles using multicomponent Gaussian fits ant several frequencies: II. individual results. *Astron. Astrophys*, **107**:527-539.

Li, J.X., Ke, X.Z., 2011. Maximum-likelihood TOA estimation of X-ray pulsar signals on the basis of Poison model. *Chin. Astron. Astrophys.*, **35**(1):19-28. [doi:10.1016/j.chinastron.2011.01.003]

Lyne, A.G., Smith, F.G., 1998. Pulsar Astronomy. Cambridge University Press, Cambridge, UK.

Ma, J., 2005. A method of autonomous orbit determination for satellite using star sensor. *Sci. China Ser. G*, **48**(3):268. [doi:10.1360/142004-23]

Manchester, R.N., Taylor, J.H., 1977. Pulsars. W.H. Freeman, San Francisco.

Psiaki, M.L., 2011. Absolute orbit and gravity determination using relative position measurements between two satellites. *J. Guid. Contr. Dynam.*, **34**(5):1285-1297.

Ray, P.S., Wood, K.S., Phlips, B.F., 2006. Spacecraft navigation using X-ray pulsars. *NRL Rev.*, p.95-102.

Ray, P.S., Sheikh, S.I., Graven, P.H., *et al.*, 2008. Deep space navigation using celestial X-ray sources. Proc. Institute of Navigation, National Technical Meeting, p.101-109.

Ray, P.S., Kerr, M., Parent, D., *et al.*, 2011. Precise gamma-ray timing and radio observations of 17 Fermi gamma-ray pulsars. *Astrophys. J. Suppl. Ser.*, **194**(2):17. [doi:10.1088/0067-0049/194/2/17]

Rinauro, S., Colonnese, S., Scarano, G., 2013. Fast near-maximum likelihood phase estimation of X-ray pulsars. *Signal Process.*, **93**(1):326-331. [doi:10.1016/j.sigpro.2012.07.002]

Sala, J., Andreu, U., Xavier, V., 2004. Feasibility Study for a Spacecraft Navigation System Relying on Pulsar Timing Information. ARIADNA Study 03/4202. European Space Agency Advanced Concepts Team.

Sheikh, S.I., 2005. The use of variable celestial X-ray sources for spacecraft navigation. University of Maryland, College Park, Maryland, United States. Available from http://adsabs.harvard.edu/abs/2005PhDT.....30S.

Sheikh, S.I., Pines, D.J., 2006. Recursive estimation of spacecraft position and velocity using X-ray pulsar time of arrival measurements. *J. Inst. Navig.*, **53**(3):149-166.

Sheikh, S.I., Pines, D.J., Wood, K.S., *et al.*, 2007. Navigational System and Method Utilizing Sources of Pulsed Celestial Radiation. Available from http://www.google.com/patents?id=31J_AAAAEBAJ.

Xu, X.B., Wu, X.J., 2003. Mean pulse analysis and spectral character study of pulsar PSR B2111+46. *Sci. China Ser. G*, **46**(1):104-112.

Zhang, H., Xu, L.P., 2011. An improved phase measurement method of integrated pulse profile for pulsar. *Sci. China Technol. Sci.*, **54**(9):2263-2270. [doi:10.1007/s11431-011-4524-8]

Zhang, H., Xu, L.P., Xie, Q., 2011. Modeling and Doppler measurement of X-ray pulsar. *Sci. China Phys. Mech. Astron.*, **54**(6):1068-1076. [doi:10.1007/s11433-011-4338-5]

Appendix A: Derivation of Eq. (29)

To simplify the derivation procedure, we substitute Λ and p_{k_n} for $\lambda(T_i, \theta)$ and $p(k_n/\varphi_v, v)$, respectively. First, we show how to derive Eq. (27). Note that

$$\log p_{k_n}=\log\left(\prod_{n=1}^{N}\frac{\Lambda^{k_n}}{k_n!}\exp(-\Lambda)\right)=\sum_{i=1}^{N}\log\left(\frac{\Lambda^{k_n}}{k_n!}\exp(-\Lambda)\right)$$
$$=\sum_{i=1}^{N}\left(k_n\log\Lambda-\log(k_n!)-\Lambda\right), \tag{A1}$$

and

$$J(\varphi_v)=-E\left(\frac{\partial^2\log p_{k_n}}{\partial{\varphi_v}^2}\right)=-\sum_{i=1}^{N}E(k_n)\frac{\partial^2\log\Lambda}{\partial{\varphi_v}^2}-\frac{\partial^2\Lambda}{\partial{\varphi_v}^2}, \tag{A2}$$

where

$$\frac{\partial^2\log\Lambda}{\partial{\varphi_v}^2}=\frac{1}{\partial\varphi_v}\partial\left(\frac{1}{\Lambda}\frac{\partial\Lambda}{\partial\varphi_v}\right)=\frac{1}{\Lambda}\frac{\partial^2\Lambda}{\partial{\varphi_v}^2}-\frac{1}{\Lambda^2}\left(\frac{\partial\Lambda}{\partial\varphi_v}\right)^2. \tag{A3}$$

By substituting Eqs. (8) and (A3) into Eq. (A2), we can easily derive Eq. (27). In Eq. (27), we have

$$\frac{\partial\Lambda}{\partial\varphi_v}=\frac{\partial[AN\eta(1+v/c)(\lambda_{\mathrm{b}}+\lambda_{\mathrm{s}}\cdot h(\varphi_v)]}{\partial\varphi_v}$$
$$\approx AN\eta\lambda_{\mathrm{s}}\frac{f_0^2}{c^2}\frac{\partial h(\varphi_v)}{\partial\varphi_v}. \tag{A4}$$

Then,

$$J(\varphi_v)=-\sum_{i=1}^{N}\frac{1}{\Lambda}\left(\frac{\partial\Lambda}{\partial\varphi_v}\right)^2$$
$$=AN\eta\lambda_{\mathrm{s}}^2\frac{f_0^2}{c^2}\int_{\mathrm{obs}}\frac{1}{b+\lambda_{\mathrm{s}}h(\varphi_v)}\left(\frac{\partial h(\varphi_v)}{\partial\varphi_v}\right)^2\mathrm{d}t, \tag{A5}$$

where

$$\left(\frac{\partial h(\varphi_v)}{\partial\varphi_v}\right)^2=\sum_{j=1}^{M}\sum_{i=1}^{M}\frac{(\varphi_v-\mu_i)(\varphi_v-\mu_j)\mathrm{C}_n^k}{\delta_k^2\delta_j^2}f_k(\varphi_v)f_j(\varphi_v)$$
$$\approx\varphi_v^2\sum_{j=1}^{M}\sum_{i=1}^{M}\frac{\mathrm{C}_n^k}{\delta_k^2\delta_j^2}f_k(\varphi_v)f_j(\varphi_v). \tag{A6}$$

The integral of Eq. (A5) is periodic, so if we neglect the contributions to the integral from fractions of a

cycle near the end point, and the number of cycles of the observation is N_c, then in each cycle we have $t=nP+t'$, where n is an integer from 1 to N_c. Hence,

$$\int_{T_{obs}} \frac{f_k(\varphi_v)f_j(\varphi_v)}{\lambda_b+\lambda_s h(\varphi_v)}\mathrm{d}t=\sum_{n=1}^{N_c}\int_{(n-1)P}^{nP}\frac{f_k(\varphi_v)f_j(\varphi_v)}{\lambda_b+\lambda_s h(\varphi_v)}\mathrm{d}t'. \quad \text{(A7)}$$

Since $h(\varphi_v)$ is periodic, all the integrals in Eq. (A7) are equal.

$$\int_{T_{obs}} \frac{f_i(\varphi_v)f_j(\varphi_v)}{b+\lambda_s h(\varphi_v)}\mathrm{d}t=N_c\int_0^P \frac{f_i(\varphi_v)f_j(\varphi_v)}{b+\lambda_s h(\varphi_v)}\mathrm{d}t'. \quad \text{(A8)}$$

Substituting Eqs. (A6) and (A8) into Eq. (A5), we can derive Eq. (29).

Appendix B: Derivation of Eq. (30)

The derivation of Eq. (28) is similar to the derivation of Eq. (27) as presented in the procedure for the derivation of Eq. (29). So, we do not go into details here. In Eq. (28),

$$\begin{aligned}\frac{\partial \Lambda}{\partial v}&=\frac{\partial[AN\eta(1+v/c)(b+\lambda_s h(\varphi_v))]}{\partial v}\\&\approx AN\eta\left(\frac{b+\lambda_s h(\varphi_v)}{c}+\lambda_s\frac{\partial h(\varphi_v)}{\partial v}\right)\\&=AN\eta\left(\frac{b+\lambda_s h(\varphi_v)}{c}+\lambda_s\frac{f_0}{c}(t-t_0)\frac{\partial h(\varphi_v)}{\partial \varphi_v}\right),\end{aligned} \quad \text{(B1)}$$

where the value of v/c is so small that it can be neglected. Substituting Eq. (B1) into Eq. (28), we obtain

$$\begin{aligned}J(v)&=AN\eta\left[\int_{t_1}^{t_2}\frac{b+\lambda_s h(\varphi_v)}{c^2}\mathrm{d}t+\int_{t_1}^{t_2}\frac{2sf_0(t-t_0)}{c^2}\frac{\partial h(\varphi_v)}{\partial \varphi_v}\mathrm{d}t\right.\\&\quad\left.+\int_{t_1}^{t_2}\frac{s^2f_0^2}{c^2}(t-t_1)\frac{1}{\lambda_b+sh(\varphi_v)}\left(\frac{\partial h(\varphi_v)}{\partial \varphi_v}\right)^2\mathrm{d}t\right]\\&=AN\eta\left[\frac{1}{c^2}\int_{t_1}^{t_2}(\lambda_b+\lambda_s h(\varphi_v))\mathrm{d}t+\frac{2sf_0}{c^2}\int_{t_1}^{t_2}(t-t_0)\frac{\partial h(\varphi_v)}{\partial \varphi_v}\mathrm{d}t\right.\\&\quad\left.+\frac{s^2f_0^2}{c^2}\int_{t_1}^{t_2}(t-t_0)^2\frac{1}{\lambda_b+sh(\varphi_v)}\left(\frac{\partial h(\varphi_v)}{\partial \varphi_v}\right)^2\mathrm{d}t\right]\\&=AN\eta\left[\frac{1}{c^2}\sum_{n=1}^{N_c}\int_0^P(\lambda_b+\lambda_s h(\varphi_v))\mathrm{d}t'\right.\\&\quad+\frac{2sf_0}{c^2}\sum_{n=1}^{N_c}\int_0^P(nP+t')\frac{\partial h(\varphi_v)}{\partial \varphi_v}\mathrm{d}t'\\&\quad\left.+\frac{s^2f_0^2}{c^2}\sum_{n=1}^{N_c}\int_0^P\frac{(nP+t')^2}{\lambda_b+\lambda_s h(\varphi_v)}\left(\frac{\partial h(\varphi_v)}{\partial \varphi_v}\right)^2\mathrm{d}t'\right]\\&=AN\eta\left[\frac{1}{c^2}\sum_{n=1}^{N_c}\int_0^P(b+\lambda_s h(\varphi_v))\mathrm{d}t'\right.\\&\quad+\frac{2\lambda_s f_0}{c^2}\sum_{n=1}^{N_c}\int_0^P(nP+t')\frac{\partial h(\varphi_v)}{\partial \varphi_v}\mathrm{d}t'\\&\quad+\frac{2\lambda_s^2f_0^2P^2}{c^2}\sum_{n=1}^{N_c}n\int_0^P t'\frac{1}{\lambda_b+sh(\varphi_v)}\left(\frac{\partial h(\varphi_v)}{\partial \varphi_v}\right)^2\mathrm{d}t\\&\quad\left.+\frac{\lambda_s^2f_0^2}{c^2}\sum_{n=1}^{N_c}n\int_0^P t'^2\frac{1}{\lambda_b+sh(\varphi_v)}\left(\frac{\partial h(\varphi_v)}{\partial \varphi_v}\right)^2\mathrm{d}t\right],\end{aligned} \quad \text{(B2)}$$

where $t=nP+t'$. When $N_c\gg1$, by far the largest contribution comes from the third term. To simplify the equation, we ignore other terms and obtain

$$\begin{aligned}J(v)&=\frac{AN\eta\lambda_s^2f_0^2P^2}{c^2}\frac{N_c(N_c+1)(2N_c+1)}{6}\\&\quad\cdot\int_0^P\frac{1}{b+\lambda_s h(\varphi_v)}\left(\frac{\partial h(\varphi_v)}{\partial \varphi_v}\right)^2\mathrm{d}t'\\&=\frac{AN\eta\lambda_s^2f_0^2}{Pc^2}\frac{T_{obs}}{3}\int_0^P\frac{1}{b+\lambda_s h(\varphi_v)}\left(\frac{\partial h(\varphi_v)}{\partial \varphi_v}\right)^2\mathrm{d}t'\\&=\frac{AN\eta\lambda_s^2f_0^2T_{obs}}{3Pc^2}\int_0^P\frac{\sum_{j=1}^{M}\sum_{k=1}^{M}\frac{\varphi_v^2\mathrm{C}_M^i}{\delta_k^2\delta_j^2}f_k(\varphi_v)f_j(\varphi_v)}{b+\lambda_s\cdot h(\varphi_v)}\mathrm{d}t'\\&=\frac{AN\eta\lambda_s^2f_0^2T_{obs}}{3Pc^2}\sum_{j=1}^{M}\sum_{k=1}^{M}\frac{4\mathrm{C}_M^k}{\delta_k^2\delta_j^2}\int_0^P\frac{\varphi_v^2f_k(\varphi_v)f_j(\varphi_v)}{b+\lambda_s\cdot h(\varphi_v)}\mathrm{d}t',\end{aligned} \quad \text{(B3)}$$

as given in Eq. (30).